

# Robust and High-Capacity Phononic Communications through Topological Edge States by Discrete Degree-of-Freedom Multiplexing

Jun Mei<sup>1,\*</sup>, Jiqian Wang,<sup>2,†</sup> Xiujuan Zhang,<sup>2</sup> Siyuan Yu,<sup>2</sup> Zhen Wang,<sup>2</sup> and Ming-Hui Lu<sup>2,‡</sup>

<sup>1</sup>*School of Physics, South China University of Technology, Guangzhou 516040, China*

<sup>2</sup>*Department of Materials Science and Engineering, National Laboratory of Solid State Microstructures, Collaborative Innovation Center of Advanced Microstructures, Nanjing University, Nanjing 210093, China*



(Received 27 August 2019; revised manuscript received 24 October 2019; published 18 November 2019)

One long-term goal of phononic communications is to achieve the controlled transport of elastic wave signals with enhanced information capacity and improved robustness, which is still challenging given the complexity of elastic waves in terms of vectorial movement and multiple polarizations. Here, we present our theoretical and experimental study of the robust transport of elastic wave signals along interfaces between distinct topological phases. These topological edge states are robust against defects and disorders because they are jointly protected by both pseudospin and valley degrees of freedom (DOFs); thus naturally providing doubled information carriers within a single channel. A topology-based beam splitter is experimentally demonstrated, where the signal's propagation path is uniquely determined and topologically protected. Edge states between distinct topological phases not only offer a route towards new topological phenomena, but also open up an avenue for the design of high-capacity and robust phononic communication devices through discrete DOF multiplexing.

DOI: 10.1103/PhysRevApplied.12.054041

## I. INTRODUCTION

The study of classical analogues of quantum topological insulators has attracted much attention in recent years [1–4], where photonic and phononic analogues of topological insulators have been proposed and demonstrated in the context of electromagnetic, acoustic, and elastic wave systems [5–32]. By engineering the spatial and time-reversal symmetries of the structural units, researchers successfully create and effectively manipulate the discrete degrees of freedom (DOFs), such as pseudospin and valley, where the analogues of quantum spin Hall (QSH) and quantum valley Hall (QVH) effects are emulated and studied. Actually, the advent of the topological phononic insulator has offered unprecedented opportunities for elastic wave manipulation and energy transport [27–32].

On the other hand, robust phononic communications with high capacity are indispensable for diverse industrial sectors, such as ocean geology and structural health monitoring, and fully enhancing the information capacity and spectral efficiency of elastic wave signals is a long-term goal in both academia and industry. In this regard, different multiplexing approaches may be applied to increase the information channels, such as wavelength multiplexing,

polarization multiplexing, and orbital angular momentum (OAM) multiplexing [33–35]. However, the existing multiplexing approaches inevitably suffer from the issue of unwanted backscattering caused by ambient defects and disorders that may substantially reduce the data transmission rate or even destroy the orthogonality between different information channels.

Here, we report the implementation of robust phononic communications through topological edge states in an intentionally designed elastic platform. With the complexity of all elastic wave polarizations and mode hybridizations fully taken into account, phononic analogues of QSH and QVH effects are emulated, where the pseudospin and valley discrete DOFs are clearly demonstrated. Due to the spin-valley-locking mechanism, edge states along the interfaces between distinct topological classes are protected jointly by both pseudospin and valley DOFs, and thus, constitute robust signal channels that are topologically protected. These edge states are not only less prone to defects and disorders, but also naturally provide doubled information carriers within a single channel. Discrete DOF multiplexing adds an extra dimension to create an additional set of data carriers, and substantially increases the information capacity of phononic communication. Our configuration suggests an alternative way towards the discovery of novel transport phenomena in topological phononics, and may serve as a building block for the coming era of large-scale phononic circuits and networks.

\*phjunmei@scut.edu.cn

†luminghui@nju.edu.cn

‡These authors contributed equally to this work.

## II. DESIGN OF THE PHONONIC STRUCTURE

To design a nontrivial phononic metamaterial, we consider a hexagonal lattice of elastic rods with width  $d$  and thickness  $t$ , as shown in Fig. 1(a), where  $a$  is the lattice constant. We use  $p$  and  $q$  to label the neighboring vertices of the hexagonal lattice, with their thicknesses denoted by  $h_p$  and  $h_q$ , respectively. When  $h_p = h_q$ , both inversion symmetry within the  $x$ - $y$  plane and mirror symmetry about the  $z = 0$  plane is preserved, and a clean and clear double-cone dispersion relation is formed at the  $K$  and  $K'$  valleys, as shown in Fig. 1(d). We note that no other modes exist around the double-cone region, which is a result of intentional design.

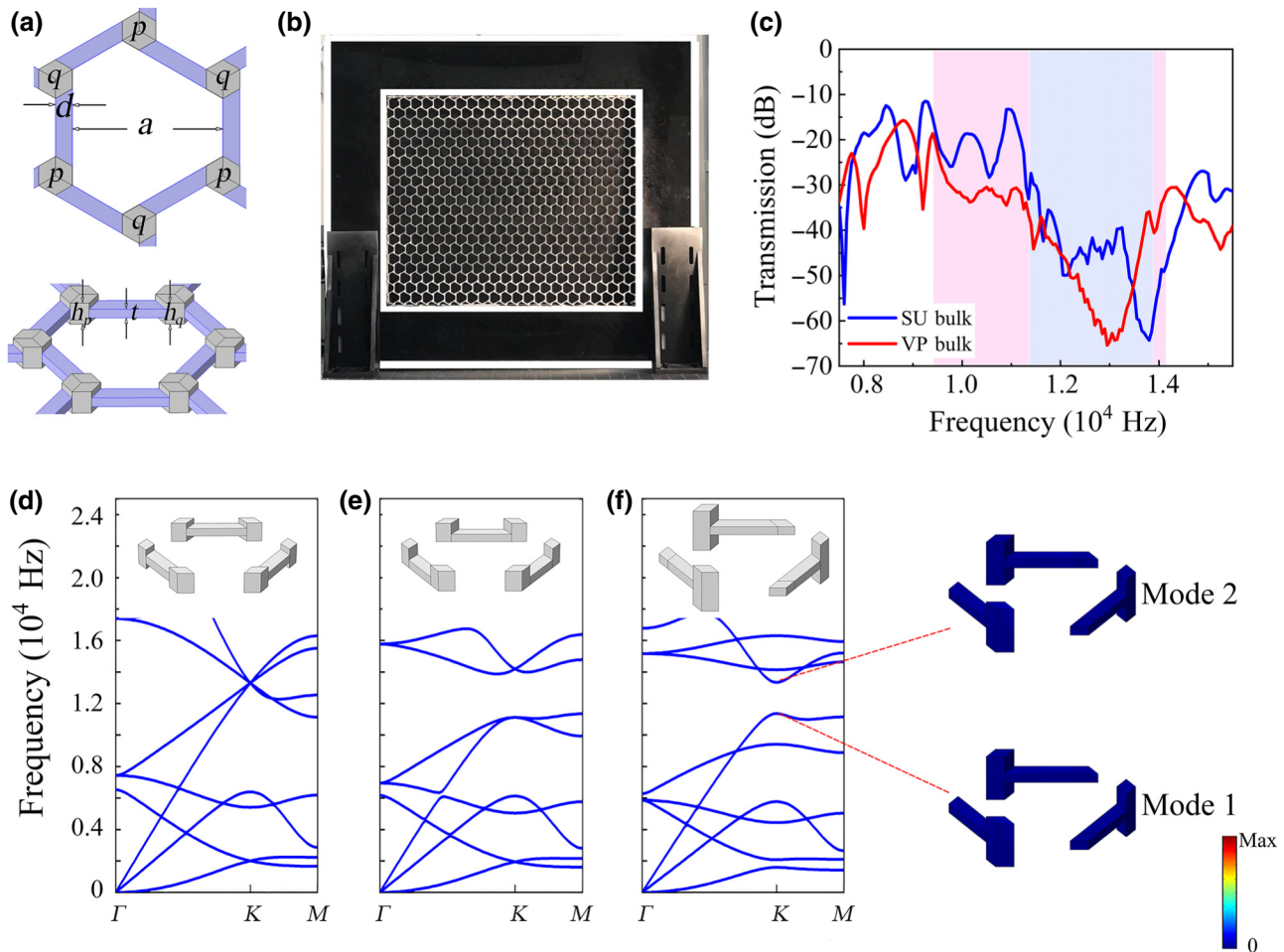


FIG. 1. Design of the elastic rod lattice with nontrivial topology. (a) Unit cell of the rod lattice;  $a = 20$  mm is the lattice constant.  $d = 2$  mm and  $t = 1.2$  mm are, respectively, the width and thickness of the elastic rod connecting two neighboring vertices (labeled as  $p$  and  $q$ ) in the hexagonal lattice. (b) Photograph of a sample used in the experiment, where the black region surrounding the sample is covered by an impedance-matched sound absorption adhesive. (c) Experimentally measured transmission spectra through the bulk lattices of QSH-like and QVH-like systems, where the shaded regions represent the corresponding band gaps for  $u_z$  ( $z$  component of displacement). (d)–(f) Schematic unit-cell configuration (upper panel) and corresponding band structure (lower panel) that exhibits a double-cone dispersion (d), a QSH gap (e), and a QVH gap (f) around the  $K$  valley, where QSH and QVH gaps overlap with each other and share the same central-gap frequency of 12.5 kHz. Inset of (f) shows that  $u_z$  is negligible for bulk modes 1 and 2, which leads to a wider QVH gap in the experimental measurement.

The metamaterial sample is fabricated from the UTR9000 acrylonitrile butadiene styrene (ABS) by three-dimensional printing, and its mass density, Young's modulus, and Passion ratio are 1133.6 kg/m<sup>3</sup>, 2946.7 MPa, and 0.31, respectively; a photograph is shown in Fig. 1(b). A sample with  $h_p = h_q = 3$  mm is schematically shown in Fig. 1(d), where the unit-cell configuration and band structure are displayed on the upper and lower panels, respectively. The fourfold degenerate eigenstates at the double-cone point can be classified according to their in-plane inversion symmetry and out-of-plane mirror symmetry. For mirror symmetry, two eigenstates at the degenerate point are symmetric ( $S$ ) modes, and the other two are antisymmetric ( $A$ ), which function as a pseudospin

DOF that effectively emulates an electron's real spin in condensed-matter physics.

We develop an effective Hamiltonian to characterize the dispersion relations and topological properties of the band structures around the  $K$  valley. For the double-cone dispersion system in Fig. 1(d), the effective Hamiltonian is  $H_0 = \omega_D I + v_A(\sigma_x \delta k_x + \sigma_y \delta k_y) \oplus v_S(\sigma_x \delta k_x + \sigma_y \delta k_y)$ , where  $\omega_D$  is the angular frequency at the degenerate point;  $I$  is the identity matrix; and  $v_S$  and  $v_A$  are the group velocities of the  $S$  and  $A$  modes, respectively.  $\sigma_{x,y}$  are the Pauli matrices acting on the orbital subspace, and  $\vec{\delta k} = (\delta k_x, \delta k_y) = \vec{k} - \vec{K}$  is the wave-vector deviation from the  $K$  point. The band structure predicted by  $H_0$  agrees very well with rigorous numerical calculations, as shown in Appendix A, which proves the validity of the effective Hamiltonian. Here, full-wave simulations are performed by using the finite-element-based software COMSOL MULTIPHYSICS.

### III. RESULTS

#### A. QSH- and QVH-like systems

Starting from the double-cone system, we shift all vertices of the hexagonal lattice along the  $z$  direction, so that the whole metamaterial is completely flat in the bottom plane, and consequently, the out-of-plane mirror symmetry is broken. An example is shown Fig. 1(e) with  $h_p = h_q = 3$  mm. It follows that a QSH-type band gap is opened around each valley due to spin-orbit coupling. Although the eigenstates are no longer purely  $S$  or  $A$  modes, their linear combination can be constructed as pseudospin up and down states [9]. For brevity, in the following discussions, we call a QSH-like system with a flat bottom (top) plane a SU (SD) system. Accordingly, the effective Hamiltonian is  $H_{\text{QSH}} = H_0 + \Delta^S \sigma_z s_z$ , where  $2\Delta^S$  is the gap width and  $s_z$  is the Pauli matrix acting on the spin subspace (see Appendix A for details). Thus, spin Chern numbers,  $C_{\uparrow/\downarrow}^S = \pm(1/2)$ , are used as the topological invariants to characterize the elastic bands below the band gap in both valleys.

When  $h_p \neq h_q$ , the in-plane inversion symmetry is broken. An example is shown in Fig. 1(f) with  $h_p = 6$  mm and  $h_q = 1.2$  mm, and a QVH-type band gap is opened at each valley. Due to the preserved in-plane  $C_3$  symmetry, a valley DOF can be defined for describing different rotating behaviors (clockwise versus anticlockwise) of Poynting vectors [31]. For brevity, we call a QVH-like system with  $h_p > h_q$  ( $h_p < h_q$ ) a VP(VQ) system. The effective Hamiltonian around  $K$  is  $H_{\text{QVH}} = (\omega_A I + \Delta_A^V \sigma_z) \oplus (\omega_S I + \Delta_S^V \sigma_z)$  (Appendix A). Thus, spin-independent valley Chern numbers,  $C_{K/K'}^V = \pm(1/2)$ , describe the topology of elastic wave bands around each valley sector, while the global Chern number must vanish due to the time-reversal symmetry.

We note that there are, in total, three kinds of elastic modes inside the metamaterial: one shear horizontal mode

plus two sets of Lamb modes. In principle, all of them can propagate along the elastic lattice. While designing the metamaterial, we ensure that a complete band gap is formed throughout the whole Brillouin zone for both QSH- and QVH-like systems, and ensure that these two gaps overlap with each other and share the same central-gap frequency, which is not a trivial task given the vectorial movement and multiple polarizations of elastic waves, as well as the possible hybridization of different modes at interfaces and domain boundaries. More discussions on the hybridization of elastic wave modes and the formation of pseudospin DOFs can be found in the Supplemental Material [36].

We experimentally measure the transmission spectra of a displacement field through both QVH- and QSH-like samples, and the results agree well with band structure calculations, as shown in Fig. 1(c). In the experiment, only the vertical component of displacement, i.e.,  $u_z$ , can be excited and detected by the sensors. It follows that the experimentally measured band gap for the QVH-like system is wider than that for the QSH-like system, as marked by light-pink and light-gray regions in Fig. 1(c), respectively. The reason is that the eigenstates on the two bulk bands near the QVH gap have a negligible  $u_z$  component [as shown in the inset of Fig. 1(f)] and cannot be excited and detected experimentally [36], which leads to a wider QVH gap.

#### B. Edge states between distinct topological phases

More interesting physics happens on the interface between distinct topological phases. Figure 2(a) shows the projected band structure along the  $x$  direction of a  $24 \times 1$  VP-SU supercell containing 12 cells on each side of the interface. A bulk band gap covering the frequency range of 11.3–13.6 kHz is obtained. Inside this bulk gap there is an edge state, as shown in by the red and blue line in Fig. 2(a). The displacement energy distribution at the green point is shown in Fig. 2(b), which exhibits an exponential decay away from the interface; thus confirming its character as an edge mode. From the dispersion relation, we can identify that the edge state corresponds to a backwards propagating spin-down state at the  $K$  valley, and a forward spin-up state at the  $K'$  valley. The propagation direction of the edge state is determined by its group velocity,  $\partial\omega/\partial k$ , around each valley. The valley-spin-locking properties of the edge state can be explained by the bulk-boundary correspondence. Take the bands around the  $K$  valley as an example: the bulk bands below the gap carry spin Chern numbers  $C_{\uparrow,K}^S = (1/2)$  and  $C_{\downarrow,K}^S = -(1/2)$  for the SU domain, and carry valley Chern numbers  $C_{\uparrow,K}^V = (1/2)$  and  $C_{\downarrow,K}^V = (1/2)$  for the VP domain. It turns out that  $C_{\uparrow,K}^S - C_{\uparrow,K}^V = 0$  and  $C_{\downarrow,K}^S - C_{\downarrow,K}^V = -1$ , which implies that only a pseudospin-down edge state can propagate backwards at the VP-SU interface around the  $K$  valley. The same principle explains

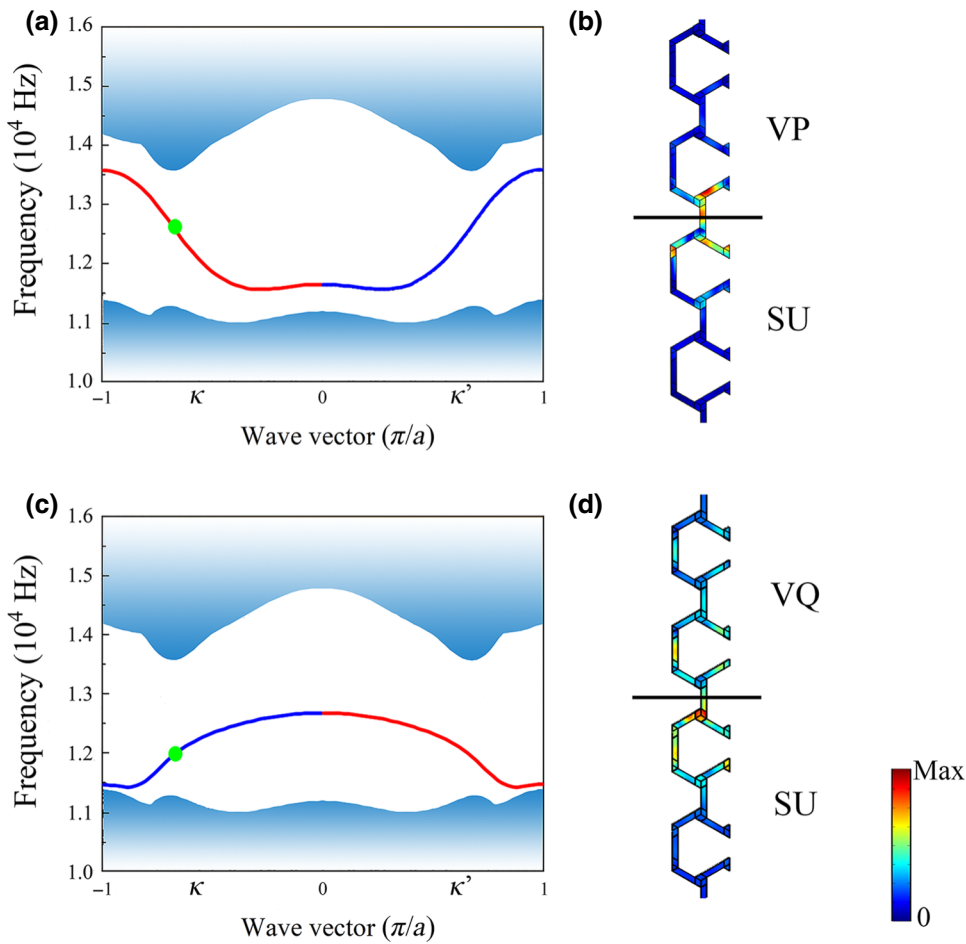


FIG. 2. Topologically nontrivial edge states along interfaces between distinct topological phases. (a) Projected band structures along the  $x$  direction for a  $24 \times 1$  VP-SU supercell consisting of 12 cells on each side of the interface. Edge state is characterized by its pseudospin DOF, with blue (red) representing spin up (spin down). (b) Displacement field distributions of the edge state at the green point, where red and blue denote the maximum and zero of the displacement's amplitude. (c),(d), The same as that shown in (a),(b), except that the supercell contains a VQ-SU interface.

the existence of a forward pseudospin-up edge state around the  $K'$  valley [10,23,30].

A similar band structure is found in Fig. 2(c), where the interface is constructed between the VQ and SU domains. Compared with Fig. 2(a), the sign of the QVH gap (denoted by  $\Delta^V$ , see Appendix A) is reversed. Thus, the valley Chern numbers change into  $C_{\uparrow/\downarrow,K}^V = -(1/2)$  for the VQ domain, while the spin Chern numbers for the SU domain remain unchanged. It turns out that  $C_{\uparrow,K}^S - C_{\uparrow,K}^V = 1$ . We also obtain an edge state at the VQ-SU interface that corresponds to a forward spin-up state at the  $K$  valley, and a backward spin-down state at the  $K'$  valley, as shown in Fig. 2(c). Comparing Fig. 2(c) with Fig. 2(a), we observe that, for an edge state propagating along the  $+x$  direction, the edge state's valley DOF changes from the  $K'$  valley to the  $K$  valley. This change provides us an effective way to selectively excite the desired edge state on the QSH-QVH interface, and implies potential applications in phononic communications.

We note that the geometrical parameters of QSH-QVH domains can influence the relative width of the bulk band gap and the shape of the edge bands. If we relax the constraints imposed by considerations of sample fabrications in the experiment, the edge states can cover the entire

frequency range of the bulk band gap (see Appendix B for details).

Edge states between distinct topological phases are robust because the valley and pseudospin DOFs are locked together. In this regard, robust edge states along the QVH-QSH interface are experimentally studied. A straight VP-SU interface is constructed in Fig. 3(a), where an excitation source is placed at the red point, and the whole sample is surrounded by perfectly matched layers (PMLs) to prevent wave reflections from boundaries. The  $u_z$  field distribution inside the red box is obtained by near-field scanning in the experiment. The results at 12.8 kHz are shown in Fig. 3(b), with experimental field-scanning data on top of numerical simulation results. They agree with each other quite well, and both of them confirm that the  $u_z$  field is highly localized around the VP-SU interface, exhibiting typical character as an edge state. The experimentally extracted transmission spectrum along the straight interface is plotted as a blue line in Fig. 3(c), where the transmission spectra through bulk materials are also plotted as dotted lines. Inside the bulk gap, the signal for the edge state is 30 dB larger than that for the bulk states, which verifies the interface's effectiveness as a waveguide channel. These edge states are robust against geometrical perturbations and/or

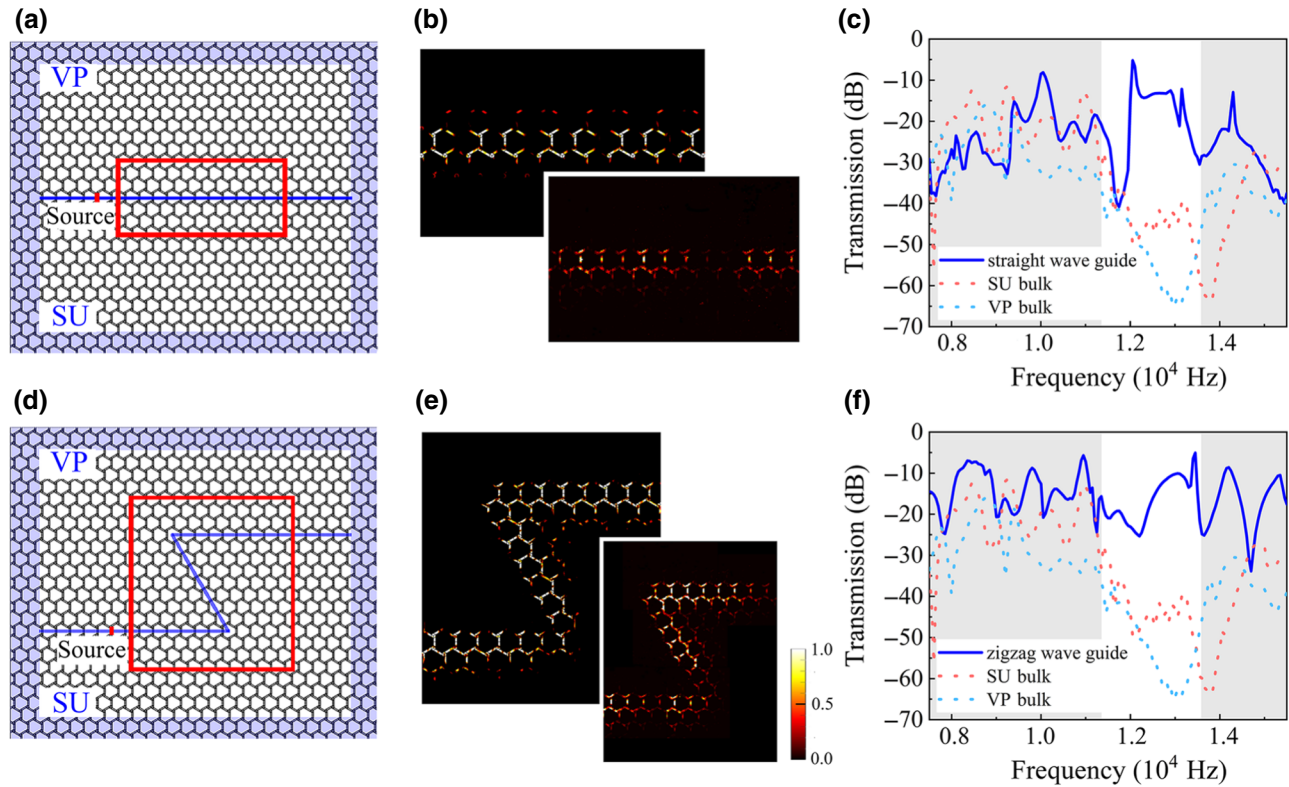


FIG. 3. Edges states along the VP-SU interface. (a) A straight VP-SU interface is constructed in a sample, which is surrounded by PMLs, as marked by the light-blue region. An excitation source is placed at the red point, and the displacement field inside the red box is scanned in the experiment. (b) Distributions of the  $u_z$  energy at 12.8 kHz, with experimental field-scanning data on top of numerical simulation results. (c) Transmission spectrum along the interface is plotted as blue line, which is orders of magnitude larger than those through bulk samples. (d)–(f) The same as those in (a)–(c) except that a zigzag interface is studied. We note that there is an intrinsic loss for the UTR9000 ABS material, which accounts for an approximate 10 dB loss in the transmission spectra in (c),(f).

defects. An example is shown in Fig. 3(d), where a zigzag interface is constructed between the VP and SU domains. Both field-scanning measurements and full-wave simulations confirm that the edge state can propagate freely along the zigzag path with negligible backscattering, as shown in Fig. 3(e). The experimentally measured transmission spectrum along the zigzag path is shown in Fig. 3(f), which is also orders of magnitude larger than those for the bulk states.

### C. Transport of elastic signals with improved robustness and enhanced capacity

One long-term goal of phononic communications is to achieve the controlled transport of elastic wave signals with improved robustness and enhanced information capacity. For improved robustness, the demonstration of topological protection against strong and random lattice disorder is shown in Fig. 4. A straight interface is constructed in three different samples, so that VP-SU, SD-SU, and VP-VQ interfaces are formed. The most important difference between them is that the VP-VQ and SD-SU interfaces stay between domains of the same topological

class, but the VP-SU interface is between domains of distinct topological classes. For the VP-SU interface, a random lattice disorder is introduced in a strong way, so that four different types of unit cells (VP, VQ, SU, and SD) are all involved, and they are randomly distributed within the 12 perturbed unit cells inside the red box, with VP (blue), VQ (red), SU (green), and SD (yellow) unit cells marked by different colors in Fig. 4. In comparison, the lattice defect for the SD-SU and VP-VQ interfaces is relatively simple and weak, where the 12 perturbed unit cells on different sides of the interface interchange their geometrical configurations with each other, e.g., a VP (VQ) unit cell is replaced by a VQ (VP) one for the VP-VQ interface.

As shown clearly in Fig. 4(a), the disorder defect has a size of  $7a \times 8a$ , which is much larger than that of the operational wavelength, and will cause significant backscattering in the absence of topological protection. According to discussions following Fig. 2 and the bulk-edge correspondence, the edge states along the VP-SU interface can be backscattered only if the pseudospin and valley DOFs are simultaneously flipped upon. In other words, these edge states are jointly protected by the pseudospin and valley indices, and thus, are naturally robust

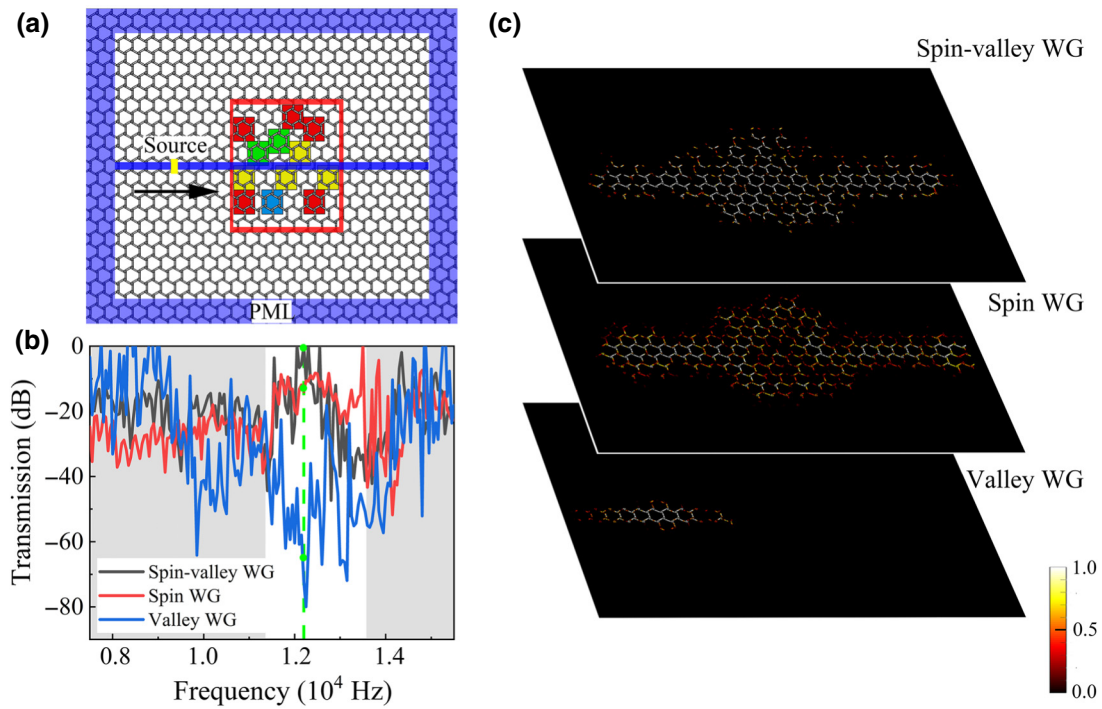


FIG. 4. Transport of elastic wave signals with substantially improved robustness. (a) A straight interface is constructed in three different samples, so that VP-SU, SD-SU, and VP-VQ interfaces are formed. For the VP-SU interface, a random disorder is introduced in a strong way, so that four different types of unit cells (VP, VQ, SU, and SD) are all involved, and they are randomly distributed within the 12 perturbed unit cells, with VP (blue), VQ (red), SU (green), and SD (yellow) unit cells marked by different colors. For the SD-SU and VP-VQ interfaces, the defect is relatively simple and weak, where the 12 perturbed unit cells on different sides of the interface interchange their geometrical configurations, e.g., a VP unit cell is replaced by a VQ one and vice versa. (b) Transmission spectra along the three interfaces are plotted as black (VP-SU), red (SD-SU), and blue (VP-VQ) lines. Green points mark the position of operating frequency at 12.2 kHz, where the distributions of the  $u$  field are displayed in (c). Clearly, edge states along the VP-SU interface are more robust against the random lattice disorders than those of VP-VQ interfaces. (c) Distributions of the  $u$  field for three different interfaces. WG denotes waveguide.

against defects and/or disorders in a way that both topological indices play their roles. The transmission spectra shown in Fig. 4(b) confirm our expectations, where we see that the signal strength along the VP-SU interface is substantially higher than that along the VP-VQ interface, and is close to that along the SD-SU interface, even when the lattice disorder for the VP-SU interface is stronger and more intense than that of the other two interfaces. In the configuration of Fig. 4, each defective unit cell is disconnected from the other; thus forming a short-range disorder instead of a smoothly varying long-range disorder. In such a situation, the intervalley scattering is strong, and the valley DOF is more prone to defects than the pseudospin DOF. This is the reason why the valley waveguide (WG) shows the lowest transmission among three types of interfaces. The distributions of the displacement field plotted in Fig. 4(c) confirm our observation. We note that the improved robustness of the edge states can be also demonstrated for a topological beam splitter that is studied both theoretically and experimentally, where the signal's propagation path is not only uniquely determined, but also

topologically protected by the discrete DOFs (please see Appendix C for more details). Thus, the robustness of the edge states along the VP-SU interface is a phenomenon that is inherently determined by the underlying spin-valley locking mechanism.

Last, but not least, we want to point out that the edge states along the VP-SU interface naturally provide doubled information carriers within a single channel. In principle, the data stream along the VP-SU interface can be divided into two parts and fed into two separate channels (i.e., VP-VQ and SU-SD channels), with each channel still topologically protected by the corresponding discrete DOF (valley or pseudospin). It means that the information capacity for a single VP-SU channel is, in fact, doubled, compared with ordinary edge states along VP-VQ or SU-SD interfaces. Here, the enhanced information capacity is enabled by discrete DOF multiplexing, which provides intrinsically orthogonal channels within each single path. This multiplexing approach can be integrated with other state-of-the-art communication modulation techniques, such as OAM multiplexing [33–35]. Information multiplexing through

discrete DOFs opens up a dimension for phononic communication, providing an enhanced data transmission rate that is important for applications in diverse industry sectors.

#### IV. CONCLUSION

We theoretically design and experimentally realize a robust transport of elastic wave signals along interfaces between distinct topological classes. Phononic analogues of QSH and QVH effects are emulated in elastic metamaterials by intentionally engineering the spatial symmetry of a unit cell. Edge states along interfaces between distinct topological classes are robust against defects and disorders due to double protection from both valley and pseudospin DOFs. The topological attributes of discrete DOFs provide intrinsically robust and independent channels, offer the unique ability to multiplex data transmission within a single edge-state channel, and substantially increase the information capacity of phononic communication. We expect that the proposed discrete DOF multiplexing approach will open up a new dimension for phononic communication, and provide an alternative solution for practical applications, when integrated with other state-of-the-art communication modulation techniques.

#### ACKNOWLEDGMENTS

J.M. would like to thank Mr. Jian Wang for helpful discussions. This work is supported by the National Natural Science Foundation of China (Grants No. 11274120, No. 11574087, No. 11625418, No. 11890700, No. 11890702, No. 51702152, and No. 51732006). J.W., X.Z., S.Y., Z.W., and M.-H.L. are also supported by the National Key R&D Program of China (Grants No. 2017YFA0303702 and No. 2018YFA0306200).

#### APPENDIX A: EFFECTIVE HAMILTONIAN

By taking into account the spatial symmetries of the elastic metamaterial, we can write the effective Hamiltonian around the  $K$  valley for the double-cone dispersion system as

$$\begin{aligned} H_0 &= \omega_D I + v_A(\sigma_x \delta k_x + \sigma_y \delta k_y) \oplus v_S(\sigma_x \delta k_x + \sigma_y \delta k_y) \\ &= \begin{pmatrix} \omega_D & v_A \delta k_- & \mathbf{0} \\ v_A \delta k_+ & \omega_D & \mathbf{0} \\ \mathbf{0} & \omega_D & v_S \delta k_- \\ & v_S \delta k_+ & \omega_D \end{pmatrix}, \end{aligned} \quad (\text{A1})$$

where  $\delta k_{\pm} = \delta k_x \pm i \delta k_y$ ,  $\vec{\delta k} = (\delta k_x, \delta k_y) = \vec{k} - \vec{K}$  is the wavevector deviated from the  $K$  point, and  $\omega_D$  is the angular frequency at the double-cone point.  $\sigma_{x,y}$  are the Pauli matrices acting on the orbital subspace.  $v_S = 34.2$  m/s and  $v_A = 20.3$  m/s represent the group velocities of symmetric ( $S$ ) and antisymmetric ( $A$ ) modes, respectively. Due to the

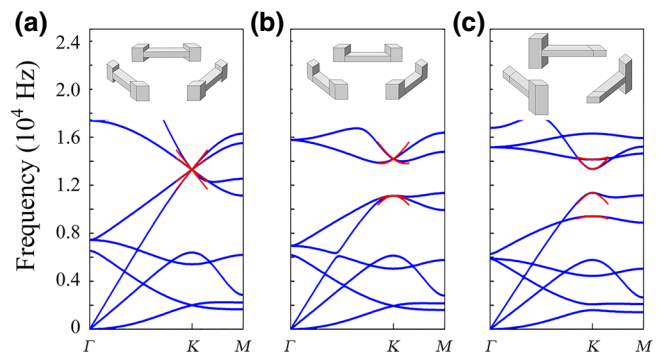


FIG. 5. Effective Hamiltonian. (a)–(c) Schematic unit-cell configuration (upper panel) and corresponding band structure (lower panel) that exhibits a double-cone dispersion (a), a QSH gap (b), and a QVH gap (c), around the  $K$  valley. Band structures predicted by corresponding effective Hamiltonians are shown in red, which agree well with the rigorous numerical results denoted in blue.

mirror symmetry of the unit-cell configuration,  $S$  modes are decoupled with  $A$  modes and  $H_0$  is a block diagonal matrix, as shown in Eq. (A1). In Fig. 5(a) the band structure predicted by the effective Hamiltonians is shown in red, which agrees well with the rigorous numerical result denoted in blue.

For the QSH-like topological system, the out-of-plane mirror symmetry is broken, as shown in Fig. 5(b), and  $S$  modes are coupled with  $A$  modes. It follows that the effective Hamiltonian around the  $K$  valley can be written as

$$\begin{aligned} H_{\text{QSH}} &= \begin{pmatrix} \omega_D + \Delta^S & v_A \delta k_- & \mathbf{0} \\ v_A \delta k_+ & \omega_D - \Delta^S & \mathbf{0} \\ \mathbf{0} & \omega_D - \Delta^S & v_S \delta k_- \\ & v_S \delta k_+ & \omega_D + \Delta^S \end{pmatrix} \\ &= H_0 + \Delta^S \sigma_z s_Z, \end{aligned} \quad (\text{A2})$$

where  $s_z$  is the Pauli matrix acting on the pseudospin subspace. As observed from Fig. 5(b), the band structure predicted by  $H_{\text{QSH}}$  agrees qualitatively well with the rigorous numerical calculations around the  $K$  valley.

For the QVH-like topological system, as shown in Fig. 5(c), the in-plane inversion symmetry is broken, and the effective Hamiltonian around the  $K$  valley can be written as

$$\begin{aligned} H_{\text{QVH}} &= \begin{pmatrix} \omega_A + \Delta_A^V & v_A \delta k_- & \mathbf{0} \\ v_A \delta k_+ & \omega_A - \Delta_A^V & \mathbf{0} \\ \mathbf{0} & \omega_S + \Delta_S^V & v_S \delta k_- \\ & v_S \delta k_+ & \omega_S - \Delta_S^V \end{pmatrix} \\ &= (\omega_A I + \Delta_A^V \sigma_z) \oplus (\omega_S I + \Delta_S^V \sigma_z), \end{aligned} \quad (\text{A3})$$

where  $\omega_A$  and  $\omega_S$  are the mid-gap frequencies for  $A$  and  $S$  modes, respectively, and  $2\Delta_A^V$  and  $2\Delta_S^V$  are the corresponding gap widths at the  $K$  valley. For  $H_{\text{QVH}}$  shown in Eq. (A3), as long as  $\Delta_A^V\Delta_S^V > 0$ , the topology of the bands below the gap around each valley can be described by the spin-independent valley Chern numbers,  $C_{K/K'}^V = \pm \frac{1}{2}\text{sgn}(\Delta_{A/S}^V)$ .

## APPENDIX B: EDGE STATES ALONG VP-SU AND VQ-SU INTERFACES

In our work, the pseudospin DOF is emulated by utilizing the spin-orbital coupling effect in the context of solid mechanics. Actually, the pseudospin up and down states in the elastic QSH system are constructed from the linear combination of the Bloch eigenstates. Since the  $z$ -directional mirror symmetry is broken, the Bloch eigenstates are no longer purely  $A$  or  $S$  mode. It follows that there is a small, but nonzero, interaction between the pseudospin up and down states, especially when the mirror symmetry is strongly broken. This is a difference between the pseudospin DOF and the real-spin DOF in condensed matter physics, where the real-spin up and down states are always rigorously orthogonal. Therefore, the picture of spin-orbital coupling is mainly valid for small perturbations in geometrical parameters, with respect to the highly symmetrical double-cone system [29]. As the perturbation becomes larger, non-negligible deviations from rigorous QSH or QVH systems emerge.

In Fig. 2, the geometrical parameters for the elastic QSH system are determined so that the whole metamaterial is completely flat in the bottom plane, which is easy to fabricate with three-dimensional printing, but, at the same time, breaks the mirror symmetry in a substantial way. Similarly, the in-plane inversion symmetry is also broken substantially in the QVH system, with  $h_p = 6$  mm and  $h_q = 1.2$  mm. The combination of these parameters produces edge states that do not cover the full frequency range of the bulk band gap.

But if we relax the strong constraints imposed by considerations of experimental fabrications, the situation is very different. In Fig. 6(b), solid lines represent the dispersion relations for the edge states along the VQ-SU and VP-SU interfaces for a different set of geometrical parameters. In particular, the vertices  $p$  and  $q$  are shifted upwards slightly by a distance of 0.35 mm for the QSH unit cell, as shown schematically in Fig. 6(a). While for the QVH unit cell, the difference between  $h_p$  and  $h_q$  decreases, so that  $h_p = 5.4$  mm and  $h_q = 1.8$  mm. In comparison, the edge bands before geometrical modification (i.e., those shown in Fig. 2) are plotted as dotted lines. Obviously, the perturbation (with respect to the double-cone system) becomes smaller after modification, and the edge states can cover the entire frequency range of the bulk band gap, as shown clearly in Fig. 6. In fact, the geometrical parameters of

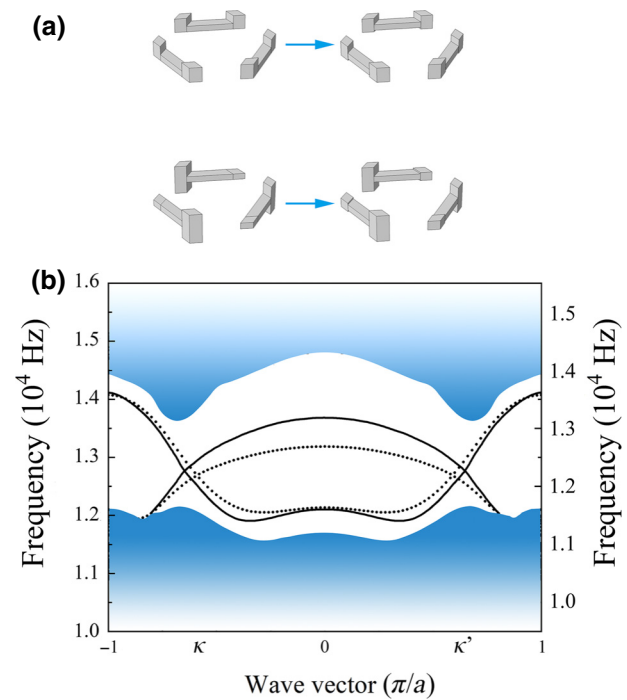


FIG. 6. Topological edge states along VP-SU and VQ-SU interfaces. (a) Modification of geometrical parameters, where the vertices  $p$  and  $q$  are shifted upwards slightly by a distance of 0.35 mm for the QSH domain (upper panel), and the difference between  $h_p$  and  $h_q$  decreases for the QVH domain, so that  $h_p = 5.4$  mm and  $h_q = 1.8$  mm (lower panel). (b) Corresponding edge bands after modification (solid lines), as well as those before modification (dotted lines).

QSH and QVH systems can influence the relative width of the bulk band gap and the shape of the edge bands, which ultimately leads to gapped or gapless edge states.

## APPENDIX C: ROBUST BEAM ROUTING PROTECTED BY NONTRIVIAL TOPOLOGY

The valley DOF (valley  $K$  and  $K'$ ) can be used to emulate a signal's bit (logic 0 and 1) in communications. In this regard, a beam splitter based on nontrivial topology is useful for practical applications. To this end, we design an arrow-shaped beam splitter that is composed of four domains: two are QVH-type (VP and VQ) and the others are QSH-type (SU and SD), as shown in Fig. 7(a). Wave energy is injected at the red point by an external excitation source. According to the discussions following Fig. 2, we know that only an edge state with pseudospin up at the  $K'$  valley can propagate along the VP-SU interface towards the right direction. Thus, the region in the black box functions as a filter that can let a signal of the edge state with specified valley and spin indices pass, but block others. Since the SD-SU interface allows the passing through of edge states with either value of pseudospin (up or down), a single-valley signal will arrive at port 1. After passing

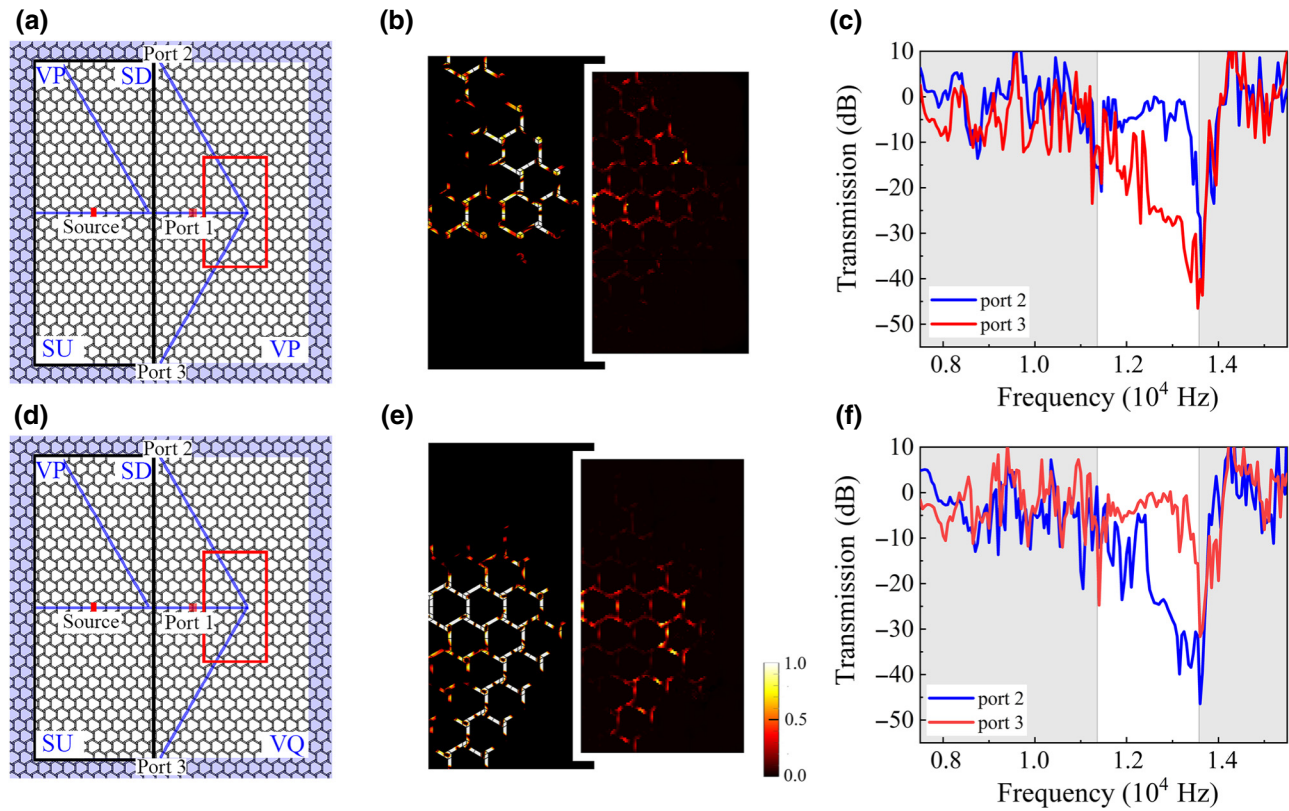


FIG. 7. A topology-based beam splitter. (a) Schematic layout of the beam splitter composed of four domains, as marked by VP, VQ, SU, and SD. Wave energy is injected at the source position, as indicated by the red point on the VP-SU interface. The whole sample is surrounded by PMLs, as marked by the light-blue region. The region in the black box functions as a filter, so that we obtain an edge mode with specified valley and spin indices at port 1. The  $u_z$  energy inside the red box is scanned in the experiment. (b) Distributions of the  $u_z$  field at 12.8 kHz, with experimental field-scanning data on top of numerical simulation results. According to the valley-spin locking mechanism, the input signal at port 1 will go to port 2. (c) Transmission spectra at ports 2 and 3, where the signal intensity at port 2 is orders of magnitude larger than that at port 3. (d)–(f), The same as that in (a)–(c), except that the VQ domain is replaced by a VP one, and the signal at port 1 will go to port 3.

through the junction, the signal will follow a path based on its valley polarization. According to the valley-spin-locking mechanism, the propagation path towards port 2 supports an edge state at the  $K'$  valley, while the path towards port 3 supports an edge state at the  $K$  valley. On the condition that the valley DOF is conserved at the intersection point, the signal will finally follow the path to port 2. This is indeed the case, as verified by both experimental field-scanning data and full-wave simulation results shown in Fig. 7(b). We also measure the transmission spectra at ports 2 and 3, and observe that the signal intensity at port 2 is about 30 dB higher than that at port 3, as can be seen in Fig. 7(c), which is consistent with the  $u_z$  field distributions in Fig. 7(b). Such a behavior of path selection is observed within the frequency range 11.3–13.6 kHz.

In a contrast sample, the VQ domain is replaced by a VP one, as shown in Fig. 7(d). As a result of this change, the propagation path towards port 2 supports an edge state at the  $K$  valley, while the path towards port 3 supports an edge state at the  $K'$  valley. In other words, paths towards

to ports 2 and 3 exchange their valley indices, compared with that in Fig. 7(a). It follows that the signal will go to port 3 after passing through the junction, due to the conservation of the valley DOF. Both simulation results and experimental data confirm our topology-based analysis, as shown in Fig. 7(e). Again, a 20 dB difference of signal intensity is observed between ports 3 and 2, as shown in Fig. 7(f).

Actually, we can draw two conclusions from Fig. 7. First, the propagation path is determined by the signal's valley polarization, which constitutes the physical foundation of this simple phononic circuit. Second, all propagation paths in Figs. 7(a) and 7(d), either towards port 2 or towards port 3, are doubly and topologically protected by the pseudospin and valley DOFs, which means that they are robust against random lattice disorders, in a similar way to those shown in Fig. 4. In short, the signal's propagation path is not only uniquely determined, but also topologically protected by discrete DOFs, which is desired for practical applications in diverse industrial sectors.

- [1] C. L. Kane and E. J. Mele, Quantum Spin Hall Effect in Graphene, *Phys. Rev. Lett.* **95**, 226801 (2005).
- [2] B. A. Bernevig, T. L. Hughes, and S. C. Zhang, Quantum spin Hall effect and topological phase transition in HgTe quantum wells, *Science* **314**, 1757 (2006).
- [3] M. Z. Hasan and C. L. Kane, Colloquium: Topological insulators, *Rev. Mod. Phys.* **82**, 3045 (2010).
- [4] X.-L. Qi and S.-C. Zhang, Topological insulators and superconductors, *Rev. Mod. Phys.* **83**, 1057 (2011).
- [5] M. C. Rechtsman, J. M. Zeuner, Y. Plotnik, Y. Lumer, D. Podolsky, F. Dreisow, S. Nolte, M. Segev, and A. Szameit, Photonic Floquet topological insulators, *Nature* **496**, 196 (2013).
- [6] A. B. Khanikaev, S. H. Mousavi, W.-K. Tse, M. Kargarian, A. H. MacDonald, and G. Shvets, Photonic topological insulators, *Nat. Mater.* **12**, 233 (2013).
- [7] L. Lu, J. D. Joannopoulos, and M. Soljačić, Topological photonics, *Nat. Photon.* **8**, 821 (2014).
- [8] J.-W. Dong, X.-D. Chen, H. Zhu, Y. Wang, and X. Zhang, Valley photonic crystals for control of spin and topology, *Nat. Mater.* **16**, 298 (2017).
- [9] T. Ma, A. B. Khanikaev, S. H. Mousavi, and G. Shvets, Guiding Electromagnetic Waves Around Sharp Corners: Topologically Protected Photonic Transport in Metawaveguides, *Phys. Rev. Lett.* **114**, 127401 (2015).
- [10] T. Ma and G. Shvets, Scattering-free edge states between heterogeneous photonic topological insulators, *Phys. Rev. B* **95**, 165102 (2017).
- [11] Z. Yang, F. Gao, X. Shi, X. Lin, Z. Gao, Y. Chong, and B. Zhang, Topological Acoustics, *Phys. Rev. Lett.* **114**, 114301 (2015).
- [12] F. Gao, H. Xue, Z. Yang, K. Lai, Y. Yu, X. Lin, Y. Chong, G. Shvets, and B. Zhang, Topologically protected refraction of robust kink states in valley photonic crystals, *Nat. Phys.* **14**, 140 (2018).
- [13] G. Ma, M. Xiao, and C. T. Chan, Topological phases in acoustic and mechanical systems, *Nat. Rev. Phys.* **1**, 281 (2019).
- [14] M. Xiao and S. Fan, Photonic Chern insulator through homogenization of an array of particles, *Phys. Rev. B* **96**, 100202(R) (2017).
- [15] R. Fleury, A. B. Khanikaev, and A. Alu, Floquet topological insulators for sound, *Nat. Commun.* **7**, 11744 (2016).
- [16] S. H. Mousavi, A. B. Khanikaev, and Z. Wang, Topologically protected elastic waves in phononic metamaterials, *Nat. Commun.* **6**, 8682 (2015).
- [17] C. He, X. Ni, H. Ge, X.-C. Sun, Y.-B. Chen, M.-H. Lu, X.-P. Liu, and Y.-F. Chen, Acoustic topological insulator and robust one-way sound transport, *Nat. Phys.* **12**, 1124 (2016).
- [18] A. Souslov, B. C. van Zuiden, D. Bartolo, and V. Vitelli, Topological sound in active-liquid metamaterials, *Nat. Phys.* **13**, 1091 (2017).
- [19] Z. Zhang, Q. Wei, Y. Cheng, T. Zhang, D. Wu, and X. Liu, Topological Creation of Acoustic Pseudospin Multipoles in a Flow-Free Symmetry-Broken Metamaterial Lattice, *Phys. Rev. Lett.* **118**, 084303 (2017).
- [20] J. Cha, K. W. Kim, and C. Daraio, Experimental realization of on-chip topological nanoelectromechanical metamaterials, *Nature* **564**, 229 (2018).
- [21] J. Lu, C. Qiu, L. Ye, X. Fan, M. Ke, F. Zhang, and Z. Liu, Observation of topological valley transport of sound in sonic crystals, *Nat. Phys.* **13**, 369 (2017).
- [22] J. Lu, C. Qiu, W. Deng, X. Huang, F. Li, F. Zhang, S. Chen, and Z. Liu, Valley Topological Phases in Bilayer Sonic Crystals, *Phys. Rev. Lett.* **120**, 116802 (2018).
- [23] Y. Kang, X. Ni, X. Cheng, A. B. Khanikaev, and A. Z. Genack, Pseudo-spin-valley coupled edge states in a photonic topological insulator, *Nat. Commun.* **9**, 3029 (2018).
- [24] M. Ezawa, Topological Kirchhoff law and bulk-edge correspondence for valley Chern and spin-valley Chern numbers, *Phys. Rev. B* **88**, 161406(R) (2013).
- [25] J. Li, A. F. Morpurgo, M. Büttiker, and I. Martin, Marginality of bulk-edge correspondence for single-valley Hamiltonians, *Phys. Rev. B* **82**, 245404 (2010).
- [26] X. Wu, Y. Meng, J. Tian, Y. Huang, H. Xiang, D. Han, and W. Wen, Direct observation of valley-polarized topological edge states in designer surface plasmon crystals, *Nat. Commun.* **8**, 1304 (2017).
- [27] M. Yan, J. Lu, F. Li, W. Deng, X. Huang, J. Ma, and Z. Liu, On-chip valley topological materials for elastic wave manipulation, *Nat. Mater.* **17**, 993 (2018).
- [28] S.-Y. Yu, C. He, Z. Wang, F.-K. Liu, X.-C. Sun, Z. Li, H.-Z. Lu, M.-H. Lu, X.-P. Liu, and Y.-F. Chen, Elastic pseudospin transport for integratable topological phononic circuits, *Nat. Commun.* **9**, 3072 (2018).
- [29] M. Miniaci, R. K. Pal, B. Morvan, and M. Ruzzene, Experimental Observation of Topologically Protected Helical Edge Modes in Patterned Elastic Plates, *Phys. Rev. X* **8**, 031074 (2018).
- [30] M. Miniaci, R. K. Pal, R. Manna, and M. Ruzzene, Valley-based splitting of topologically protected helical waves in elastic plates, *Phys. Rev. B* **100**, 024304 (2019).
- [31] J. Wang and J. Mei, Topological valley-chiral edge states of Lamb waves in elastic thin plates, *Appl. Phys. Express* **11**, 057302 (2018).
- [32] X. Zhang, M. Xiao, Y. Cheng, M.-H. Lu, and J. Christensen, Topological sound, *Commun. Phys.* **1**, 97 (2018).
- [33] C. Shi, M. Dubois, Y. Wang, and X. Zhang, High-speed acoustic communication by multiplexing orbital angular momentum, *Proc. Natl Acad. Sci. USA* **114**, 7250 (2017).
- [34] Y. Yan, G. Xie, M. P. J. Lavery, H. Huang, N. Ahmed, C. Bao, Y. Ren, Y. Cao, L. Li, Z. Zhao, A. F. Molisch, M. Tur, M. J. Padgett, and A. E. Willner, High-capacity millimetre-wave communications with orbital angular momentum multiplexing, *Nat. Commun.* **5**, 4876 (2014).
- [35] L. Gong, Q. Zhao, H. Zhang, X.-Y. Hu, K. Huang, J.-M. Yang, and Y.-M. Li, Optical orbital-angular-momentum multiplexed data transmission under high scattering, *Light: Sci. Appl.* **8**, 27 (2019).
- [36] See the Supplemental Material at <http://link.aps.org/supplemental/10.1103/PhysRevApplied.12.054041> which contains a discussion on the pseudospin DOF in the elastic metamaterial.